technologies

MDPI

Article

Optical Particle Tracking in the Pneumatic Conveying of Metal Powders through a Thin Capillary Pipe

Lorenzo Pedrolli [1,*], Luigi Fraccarollo [2], Beatriz Achiaga [1] and Alejandro Lopez [1,*]

[1] Faculty of Engineering, University of Deusto, 48007 Bilbao, Spain; beatriz.achiaga@deusto.es
[2] Dipartimento di Ingegneria Civile, Ambientale e Meccanica, Faculty of Engineering, University of Trento, 38123 Trento, Italy; luigi.fraccarollo@unitn.it
* Correspondence: l.pedrolli@deusto.es (L.P.); alejandro.lopez@deusto.es (A.L.)

Abstract: Directed Energy Deposition (DED) processes necessitate a consistent material flow to the melt pool, typically achieved through pneumatic conveying of metal powder via thin pipes. This study aims to record and analyze the multiphase fluid–solid flow. An experimental setup utilizing a high-speed camera and specialized optics was constructed, and the flow through thin transparent pipes was recorded. The resulting information was analyzed and compared with coupled Computational Fluid Dynamics-Discrete Element Modeling (CFD-DEM) simulations, with special attention to the solids flow fluctuations. The proposed methodology shows a significant improvement in accuracy and reliability over existing approaches, particularly in capturing flow rate fluctuations and particle velocity distributions in small-scale systems. Moreover, it allows for accurately analyzing Particle Size Distribution (PSD) in the same setup. This paper details the experimental design, video analysis using particle tracking, and a novel method for deriving volumetric concentrations and flow rate from flat images. The findings confirm the accuracy of the CFD-DEM simulations and provide insights into the dynamics of pneumatic conveying and individual particle movement, with the potential to improve DED efficiency by reducing variability in material deposition rates.

Keywords: particle tracking; pneumatic conveying; flow irregularities; measurement

Citation: Pedrolli, L.; Fraccarollo, L.; Achiaga, B.; Lopez, A. Optical Particle Tracking in the Pneumatic Conveying of Metal Powders through a Thin Capillary Pipe. *Technologies* **2024**, *12*, 191. https://doi.org/10.3390/technologies12100191

Academic Editor: Juan Gabriel Avina-Cervantes

Received: 29 July 2024
Revised: 11 September 2024
Accepted: 16 September 2024
Published: 3 October 2024

1. Introduction

In additive manufacturing, particularly Directed Energy Deposition (DED), understanding the pneumatic conveying characteristics of metal powder feedstock is crucial. The powder is fed into the pneumatic system using metering equipment that ensures a uniform gas/powder mixture flow. Upon reaching the nozzle, various configurations such as off-axis, discrete coaxial, continuous coaxial, annular continuous, and discrete laser beam are possible [1]. Figure 1 illustrates a discrete coaxial nozzle with four channels conveying metallic powder towards the melt pool, where the red-highlighted channels show the final part of the conveying path.

Irregularities in track width in the deposition direction and roughness profiles, as reported by Dadbakhsh et al. [2], motivate this investigation. Variations in the powder feed can impact the quality of the deposited material, while previous studies often consider time-averaged powder flows [3,4], the mass flow rate variability in pneumatic conveying systems is a well-documented phenomenon [5–8]. Several factors influence pneumatic conveying flow, and they are thoroughly discussed in the literature [9–11], and remain an active area of research due to the variability in powder characteristics and application-specific requirements.

Self-induced and regular variations in pneumatic conveying flow can affect particle velocity and instantaneous powder mass flow rate, directly influencing the material deposition rate in DED processes. Zhou et al. [12] studied larger-scale pneumatic conveying systems, observing pulsating flow phenomena and periodic flow regimes in a rectangular

pipe, both experimentally and through simulations. Self-excited flow oscillations can be simulated with four-way coupled simulations, but not when the particle effect on the carrier flow is neglected. In CFD-DEM simulations of a horizontal channel by Zhao [13], uniform particle motion and velocity were observed under 1-way coupling, whereas considering particle influence on the fluid motion (two-way coupling) resulted in visible bands of higher and lower particle concentration.

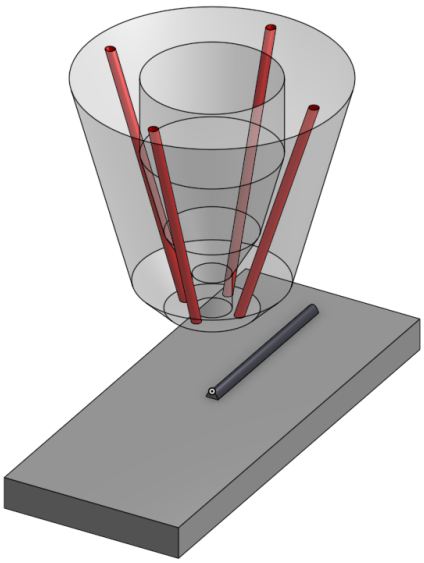

Figure 1. Example draft of a typical discrete Laser Metal Deposition (LMD) nozzle with four converging powder conveying channels (highlighted in red). A central channel allows the passage of the laser and the shielding gas.

Existing literature on Metal Deposition (LMD) nozzle systems which employs a Lagrangian model for the powder phase mostly analyzes the process using Multi-Phase—Particle In Cell (MP-PIC) [3,14] or Discrete Particle Models (DPMs) with 1-way coupling [14], motivated by the low particle loading in the system. Previous studies report how the particle–particle interaction in Computational Fluid Dynamics—Discrete Element Modeling (CFD-DEM) simulations leads to the formation of clusters [5,15], and therefore powder mass flow rate fluctuations. Even though the MP-PIC model finds most of its applications in large reactor models, it is used in the modeling of the pneumatic conveying of solids [16].

Since the referenced literature deals with horizontal channel flow, this experiment is also conducted in this orientation. Future work will focus on analyzing flow in different orientations, including vertical configurations, and will also capture the flow exiting the conveying pipes for a comprehensive analysis.

This study specifically focuses on analyzing the pneumatic conveying flow of the metallic powder used in LMD equipment. Even under diluted flow conditions, the main objective is to validate the emergence of self-induced and regular variations in the powder mass flow rate. The pipes used are scaled to represent realistic LMD systems, ensuring practical relevance.

In addition to the experimental analysis, the results are compared with expected outcomes from CFD-DEM simulations [17], which allows us to assess the agreement between experimental and simulation data. This validation framework is critical for improving the reliability of simulation-based approaches in LMD process analysis.

The key contributions of this work are as follows:

- Development of a detailed methodology for analyzing pneumatic powder flow in LMD systems.
- Confirmation of self-induced and regular variations in powder mass flow rate under diluted flow conditions.

- Comparison of experimental results with CFD-DEM simulations, establishing a validation framework for future studies.

This paper reports the development of the methodology used for these investigations, with particular emphasis on the experimental setup and the analysis tools developed to characterize the powder flow dynamics in similar systems.

2. Experimental Setup

The objective of this work is to propose a reproducible method for obtaining particle velocities and other characteristics of the conveyed powder flow using particle tracking. Previous experimental works, such as those compiled by Sommerfeld et al. [15], have focused on larger-scale systems, often using rougher pipe conditions and larger particle sizes. In contrast, our method focuses on smaller-scale systems with smooth pipe conditions and smaller particles, allowing for a more precise determination of particle size and its influence on flow properties. This advancement enables the effective calculation of particle velocities and mass flow rate.

While Sommerfeld et al. [15] present a comparative table of previous works, the conditions used in this study differ significantly due to the smaller particle size and smoother pipes, making direct comparisons challenging. Nonetheless, the improvements in our approach, particularly regarding the accurate measurement of individual particle velocities, represent a substantial enhancement over the previous methods.

2.1. Conveying Circuit

Experiments were conducted using circular, borosilicate glass pipes of $d = 1.15$ mm at different gas flow rates of $\dot{V} = [0.4,\ 0.6,\ 0.8]$ L/min. The material is AISI 316L stainless steel, in the commercial form *Oerlikon MetcoAdd 316L-D* [18] with a nominal Particle Size Distribution (PSD) described by $D_{90} = 106$ µm and $D_{10} = 45$ µm. These values can be compared with the PSD determined experimentally, in Section 4.1.

The schematic of the pneumatic conveying circuit is presented in Figure 2. The central part of the circuit is the borosilicate glass pipe, of which the wall thickness is 0.2 mm. Clean and dry nitrogen gas is supplied by a canisterm, not represented, and metered through a flow regulator. Powder is fed into the system by a custom designed rotary feeder valve, which is then coupled to the transparent pipe. The powder is then reclaimed using a small cyclone separator, the nitrogen gas is exhausted through a filter.

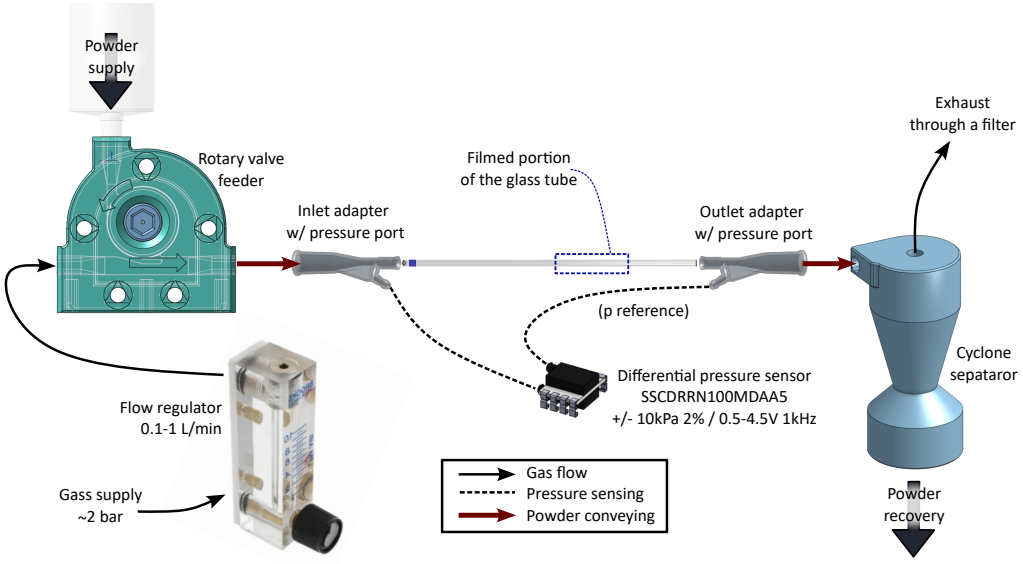

Figure 2. Schematic of the pneumatic conveying circuit used in the experiment.

The central part of the circuit is the borosilicate glass pipe, of which the wall thickness is 0.2 mm.

2.1.1. Glass Pipe Coupler

The development of the system involved the design of small-scale couplers for the pipe. Figure 3 shows the finished result, manufactured using Stereolitography 3D printing. The internal channels have larger nominal sizes to account for manufacturing tolerances. The couplers were printed in a batch and manually selected to ensure the best fit with the pipe's internal channel.

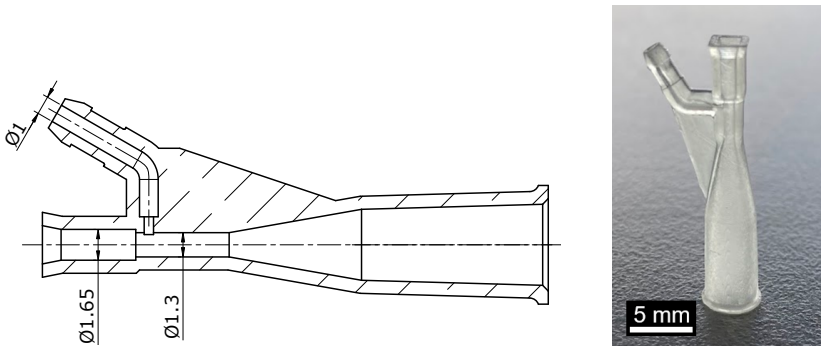

Figure 3. One of the couplers. The opening of the static pressure port in the manufactured part is barely visible to the naked eye. A section view presents the internal channels. The conic section is used to fit the coupler to the flexible pipe.

The same technology allowed to manufacture and iterate on a rotary valve feeder. This element shows areas of improvement, but it allowed to effectively feed the powder in the circuit for the short duration of the measurements.

The gas supply is provided by a high-pressure tank of clean, dry, pure nitrogen gas. This high-purity gas supply ensures that the contamination from moisture or oils is not present, and completely avoids a compressor which might send vibrations down the gas line. A needle regulator was used to set the gas flow rate.

2.1.2. Sensors Integration

The circuit schematic in Figure 2 shows that the pressure ports are connected to a Honeywell SSCDRRN100MDAA5 [19] piezo-resistive differential pressure sensor. The sensor provides a 0.5–4.5 V analog output, with a full scale of $\pm$10 kPa. The 3D-printed couplers (see Figure 3), were designed to have a lateral port to measure the static pressure at the inlet and outlet of the pipe. A batch of couplers was printed, selecting those that provided the best alignment of the central channel between the glass pipe and the coupler. Therefore, minimum disturbance is expected when measuring the static pressure.

The calibrated output values are updated at 1 kHz and recorded using a 14-bit USB oscilloscope. The sensor provides an accuracy of $\pm$0.25% FSS (Full-Scale Span) in the same measurement period. When accounting for other effects (temperature variation, voltage offset, calibration, orientation respective to gravity), the manufacturer declares a total error band of $\pm$2% FSS. Consequently, while the absolute value of the differential pressure can be determined within $\pm$0.2 kPa, the accuracy for tracking pressure changes over time remains at $\pm$0.025 kPa.

The second channel of the oscilloscope was connected to a Vishay BPW34 photodiode, with a sensing area of 3 $\times$ 3 mm. A simple voltage divider and amplifier were used as preconditioning circuit.

2.2. Camera Configuration

A Phantom VEO 640L (https://www.phantomhighspeed.com/products/cameras/veo/veo640 (accessed on 20 July 2024).) high-speed camera is visible in the setup of Figure 4; the circuit schematic is presented in Figure 2. The camera carries a CMOS (global shutter) sensor, with 256 $\times$ 1600 px, and each pixel is a square of side 10 µm. The camera has an

electronic global shutter which duration can be selected independent of the fps. With good illumination, the optimal balance was found at around 10 µs; longer times result in better illumination but the particles form a streak if they are moving too fast.

The camera is equipped with a 25 mm f/2.8 2.5-5X Ultra Macro lens, Wayne, NJ, USA. Compared with similar models, it has a good aperture (F2.8), meaning it is expected to deliver more light to the sensor compared to other alternatives. The aperture can be reduced (down to F16) to improve the depth of field. Given the camera's sensor size of 25.6 × 16 mm (circa APS-C), it has a pixel size of 10 µm. The recording window for the circular and square pipes was selected at 1280 × 400 px, with a sample rate of 10,000 fps. The resulting physical image resolution attainable using the described camera and lens is reported in Table 1.

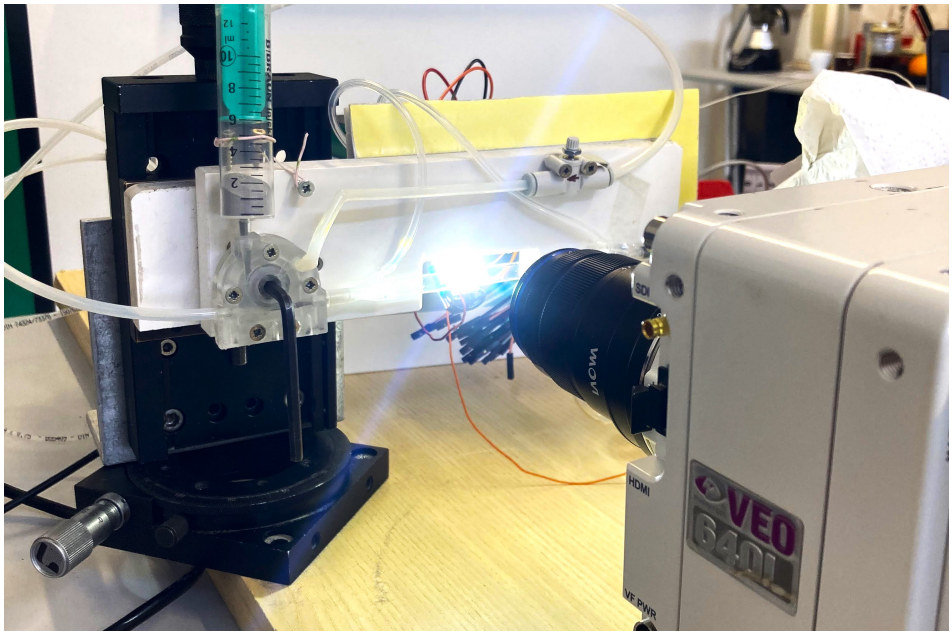

Figure 4. Photo of the setup for the pneumatic conveying experiment.

Table 1. Field of view and pixel size that can be provided by the camera and lens setup at different magnification levels.

Magnification	Field of View	Pixel Size
2.5×	10.24 × 6.4 mm	4 µm
5×	5.12 × 3.2 mm	2 µm

The camera is also mounted on a slider, which allows it to move closer or farther from the pipe in a precise manner, changing the focus. Especially with full aperture, the field of view is quite shallow, and it is crucial to put the focus plane on the center of the pipe. The pipe assembly is moved in order to align its mid-plane with the recording plane. The image is captured around the middle of the pipe length, limiting edge issues. The resulting pictures are of good quality and an example with minimal post-processing is shown in Figure 5.

Figure 6 presents a detailed view of a group of medium-sized particles, where the pixel size is approximately 3 µm. The image resolution allows a direct estimation of the PSD, given the expected particle diameters from the powder's datasheet [18]. The exposure, or the time when light is actually collected by the sensor, must be relatively short to avoid blur in the direction of motion. An exposure of around 10 µs almost completely eliminated the streaks while maintaining a good image luminosity with an aperture between F5.6 and F8.

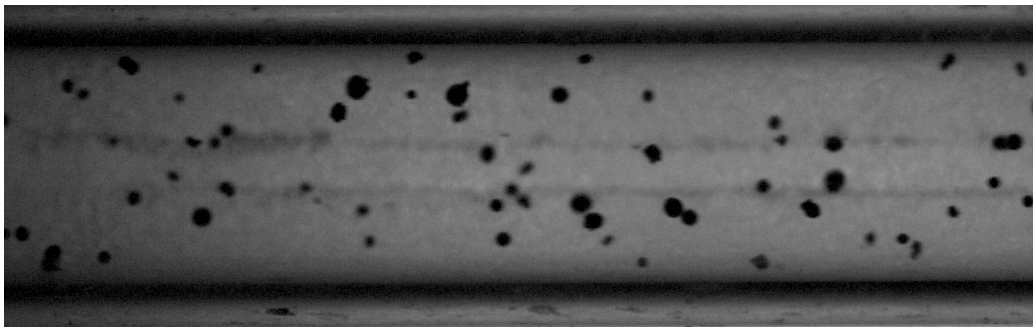

Figure 5. Circular pipe (∅1.15 mm), 1280 × 400 px, exposure 6.5 µs, aperture F8, sample rate 10,000 fps.

The illumination of the section of interest is directly from the side opposite the lens. A high-powered LED light shines light towards the pipe and to the lens. It is extremely bright, and it is advisable to use some level of PPE when on. A layer of frosted acrylic sheet in front of the LED diffuses the light, resulting in sharper images and a more uniform background.

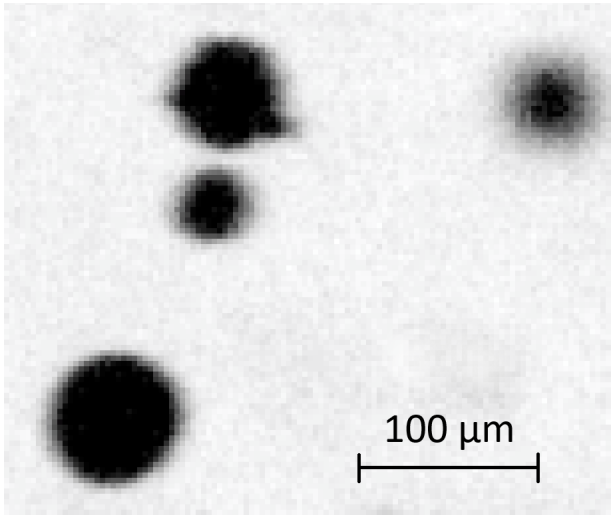

Figure 6. Detailed view of four particles captured in Figure 5.

3. Particle Tracking (PT)

Figure 5 reports static snapshots of the flow conditions. To track the movement of particles over time, the positions should not change excessively from one frame to another. The image sequence is presented in Figure 7, where the particle movement is immediately evident. Each recording is in the order of 10^4 frames, for a total duration of around 1 s. Counting all the particles present in all the frames, the number of spots to be considered for the tracking procedure is approximately 3×10^5.

The videos captured using the setup described in this section were analyzed as an "image stack", or a sequence of 8-bit grayscale images, in the image-processing software Fiji/ImageJ (version 2.9.0) [20]. In the pre-processing step, the original video is rotated, cropped, and transformed into a black-and-white binary mask according to a brightness threshold. More advanced image filtering and segmentation methods are available in the software and were tested, but were superfluous thanks to the camera and lighting setup, which already provide very easily identifiable spots. This work refers to particles as the physical, 3D objects that compose the powder; spots are their 2D shadows captured on each image of the high-speed video.

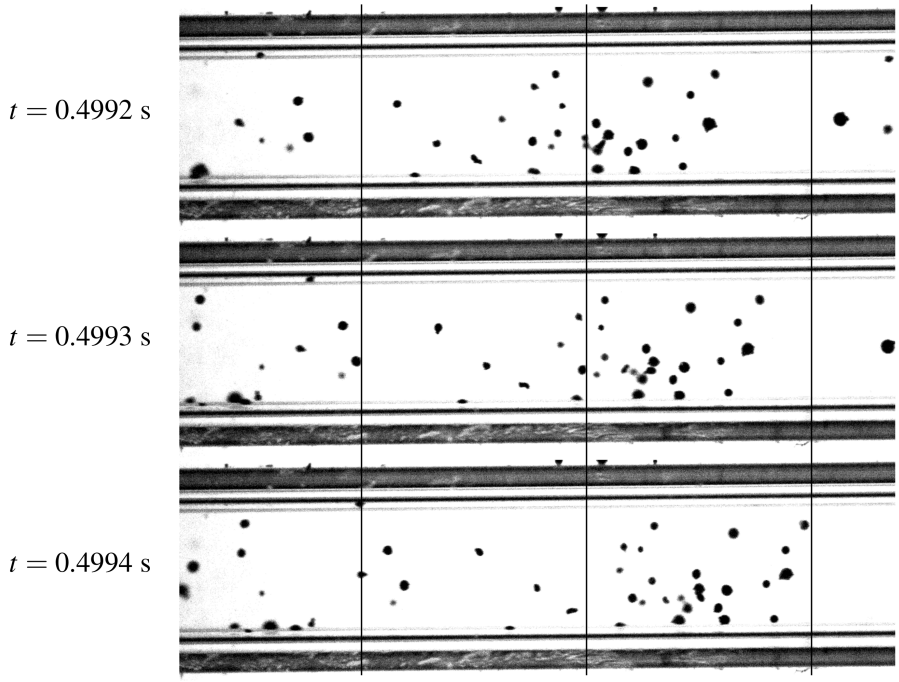

Figure 7. Image sequence from the recordings. The gas flow in this case is 0.4 L/min. Notice the particle movement relative to the vertical grid lines.

Particle tracking and analysis were performed using TrackMate (version v7.10.0) [21], an additional plugin to Fiji. Essential to this work is its implementation of the linear motion tracker, which can deal with particles moving with a roughly constant velocity. It is based on the Linear Assignment Problem (LAP) framework [22], which approximates multiple-hypothesis tracking using a linear assignment problem; a cost matrix penalizes the least likely movements. It was developed mostly to track the Brownian motion of bacteria, but it is used in TrackMate to track fast-moving objects using a Kalman filter strategy: the particle tracks are analyzed, in the hypothesis of mostly linear motion, and a prediction is made for the subsequent steps. If there is a particle within a tolerance of the expected landing spot, a new segment (called edge) is added to the track. With enough information, the implementation can track the particle even if it is not visible for a predefined number of steps. Penalties can be assigned to several conditions, namely the spot area and perimeter, increasing the robustness of the system to track objects that are not expected to change in shape and size; lower weights can be assigned to loosen the condition, accounting for rotating particles. The tracker was modified in the scope of this work, in order to improve the track initialization step, as reported in Appendix A. Conveniently, the spot identification step of TrackMate records the geometric descriptor of each spot: area and perimeter are used to calculate the equivalent diameter, along with other shape descriptors like circularity, Feret diameters, and ellipsoid axes. The post-processed high-speed videos result in four different files, as follows:

`spots.csv` containing the position of each spot in time and space, a unique numeric identifier (ID), geometrical information (area, perimeter, circularity, ...), as well as the ID of the track it is included in.

`edges.csv` specifies the source and target spot IDs, the displacement and duration (which may be multiples of the frame Δt), the speed, and again the ID of the track it is included in.

`tracks.csv` specifies the overall track information, like total track duration, average speed, and more.

`allspots.csv` is the same as `spots.csv`, but it also includes the spots that do not participate in a track, therefore is preferred when determining the concentration.

3.1. Occlusion

At this stage, no specific assumptions were made regarding the depth of the pipe along the camera axis. However, occlusion significantly impacts the accuracy of volumetric density measurements. Spinewine et al. [23] offer a detailed analysis of occlusion effects observed when imaging particles at increasing depths within a channel. Their work depicts the distribution of visible particle centers relative to depth (perpendicular to the wall) for two distinct concentrations (57% and 26%). The figure clearly demonstrates that the observable particle volumetric density is merely a fraction of the actual volumetric density, with the discrepancy widening as the depth from the camera's viewpoint increases.

3.2. Tracking Verification

The particle-tracking software was tested on a simulated dataset to estimate the performance of the technique, having control of all possible variables. The model discussed in the article by Pedrolli et al. [17] was adjusted to replicate the flow in conditions similar to the experiment. The simulation yielded a series of datasets containing particle positions and velocities recorded at intervals of 10^{-4} s, matching the framerate of the high-speed videos. These datasets serve as the baseline, or "ground truth," for assessing the error introduced during the particle-tracking phase of the analysis.

Using Paraview [24], the simulation output was post-processed into a series of images, replicating those captured by the experimental setup. In these images, particles are depicted as dark circles against a white background, as shown in Figure 8A, occasionally overlapping. Overlapping particles pose a challenge for tracking. To address this, the chosen approach involves selecting only fully visible particles, employing the Kalman filter strategy implemented in TrackMate [21]. Figure 8B illustrates the same frame as Figure 8A, overlaying the spots utilized in tracking and their corresponding tracks. It is worth noting that while the tracks may be incomplete, they provide sufficient data for velocity analysis. The relative position of the particles in the direction orthogonal to the plane is represented by Figure 8C, where darker particles are farther from the observer, evidencing the particle overlapping.

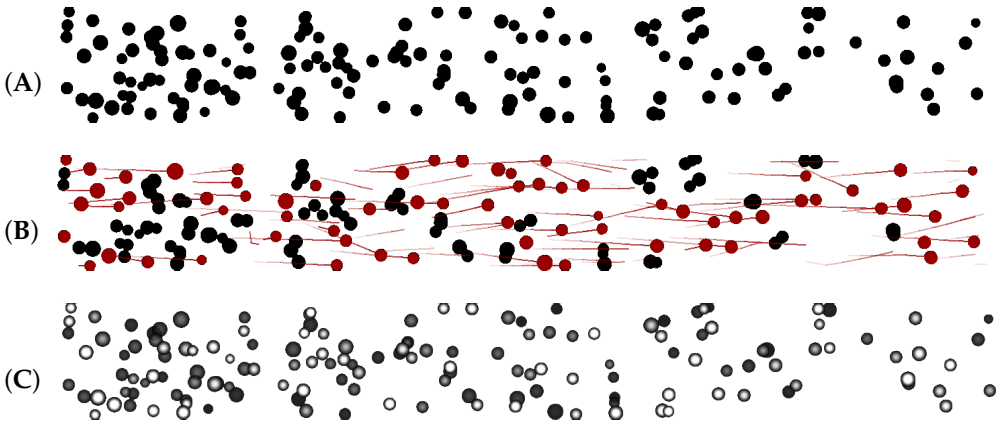

Figure 8. Example snapshot of the simulated particle tracking (sPT). (**A**) Particles represented as uniformly colored dark circles. The tracking result in (**B**) highlights the tracked spots and their respective tracks (backwards in time). The shaded representation in (**C**) displays particle overlapping, with darker particles being farther from the observer.

The tracking information was exported from TrackMate as CSV files containing all the *Spots*, *Edges*, and *Tracks*. Tracks consist of a series of edges, each defined by an origin and target spot. These elements are interconnected through identifier numbers (IDs), with edges containing the IDs of their respective origin and target spots.

Matlab (version 2023a) scripting was the tool of choice to analyze the results, and get to the values of interest. Most relevant for the LMD process is the instantaneous mass flow rate of metallic powder. The resulting values are depicted in Figures 9 and 10. The

values labeled as *OpenFoam data* refer to the direct extraction of particle diameters and velocities from the simulation. Both the results of the tracking and the simulation's raw dataset were processed the same way, for consistency. The area concentration from the particle tracking is the direct measurement of the dark spots against the light background, essentially equivalent to counting the black vs. white pixels of the binary map represented in Figure 8A.

Figure 9 displays the difference between the ground truth (*OpenFOAM data*) and the simulated *particle tracking*. In both cases, area and volume fraction concentrations, there is a discrepancy. The volume fraction discrepancy was plotted as a function of the volume fraction ϕ determined using the particle tracking and the expected one determined by the simulation. This results in a clear linear relationship. This is easily explained by the occlusion phenomena (see Section 3.1), and therefore the line passes through the origin since the occlusion error should tend to zero for very low concentrations. Compared to the work by Spinewine et.al. [23], in this case, the concentration is much lower, and therefore the linear fit will be used directly to correct the volumetric concentration and then calculate the mass flow rate.

Knowing the density of the particle material ρ_s, assuming uniform density within each particle, the mass flow rate of the solid particles is calculated as

$$\dot{m} = \rho_s (V_{tot} \cdot \phi) \hat{v_Z} \tag{1}$$

where $\hat{v_Z}$ is the average velocity of the particles along the pipe, determined using the particle tracking of Figure 8. The total volume of the solid particles is expressed by the total observed volume V_{tot}, multiplied by the volumetric concentration ϕ. Without applying the correction to the volume, this results in the mass flow rate reported in Figure 10. This diagram also reports the average particle velocity and the standard deviation intervals in of the velocities in the frame, which coincide almost perfectly (the average error is less than 1%). The flow rate corrected using the linear fit is not represented in the figure as the two lines effectively overlap, and the error is also less than 1%.

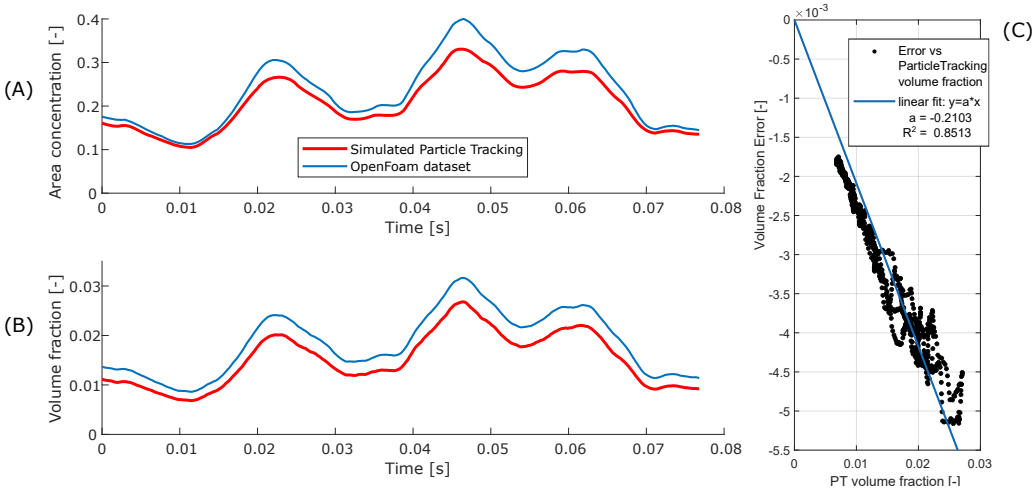

Figure 9. Simulated: solids concentration in the simulated flow, both as projected area (**A**) and volumetric (**B**). The values coming from the particle-tracking method are compared with those of the raw dataset. All data were filtered with a 2 ms moving average. (**C**) The error in the estimated volume fraction is fitted by a line passing through the origin.

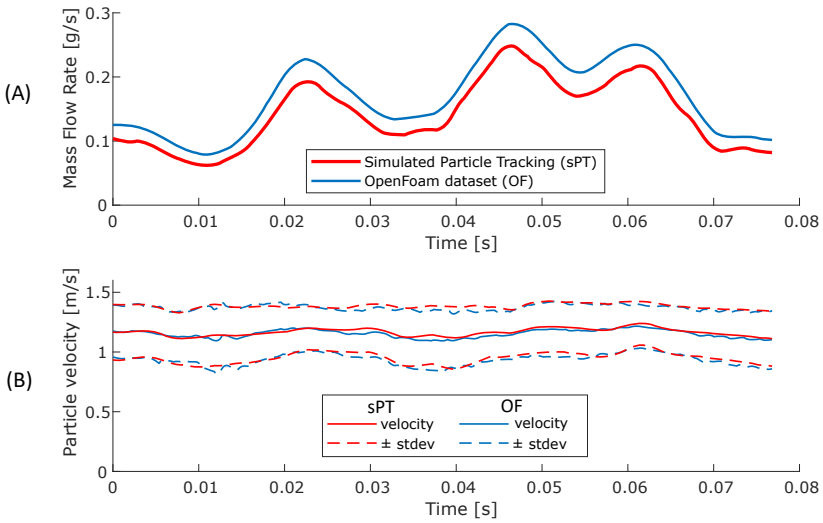

Figure 10. Simulated: particle average velocity and standard distribution in the observed section of the simulated flow over time (**A**), and calculated mass flow rate (**B**). The data were filtered with a 2 ms moving average. These data were not corrected with the information of Figure 9.

4. Results

The experimental particle-tracking (ePT) results are discussed in this section. For the main presented case, the flow rate of clean and pure Nitrogen gas was set to 0.8 L/min, which corresponds to the average gas velocity $\overline{u} = 12.8$ m/s average gas velocity. In this case, the Reynolds number is

$$Re = \frac{\rho_g \overline{u} d}{\mu} = 971.3 \tag{2}$$

where, considering the standard conditions of 20 ºC and 1 atm, $\rho_g = 1.160$ kg/m^3 is the gas's density, $d = 1.15$ mm is the pipe diameter, $\mu = 17.58 \times 10^{-6}$ Pa · s. This low value denotes that a laminar flow is expected.

The number of items for each type generated by the particle-tracking code from the experimental recordings is presented in Table 2; the files are available as an open repository [25]. The table also reports the average number of spots contained in each frame. If not indicated otherwise, the values over time are filtered using a moving average over 2 ms, the number of spots in the averaging window is indicated in the table.

Table 2. Number of individual items recorded in the experiments by the particle-tracking code [25].

Case:	**0.8 L/min**	**0.6 L/min**	**0.4 L/min**
Spots	336,828	336,036	179,099
Edges	205,450	247,300	153,576
Tracks	57,951	45,560	20,463
Total time [s]	0.7100	0.7993	0.8066
Spots in frame	47.5	42.0	22.2
Spots in 2 ms	950	841	444

4.1. Particle Size Distribution

The PT algorithm uses the spot area and other metrics to find the most likely trajectories. As indicated, all this information is available in the output files. When determining the Particle Size Distribution, it is appropriate to use the method described in Appendix B to correct for the occlusion. Finding a PSD skewed towards larger particle size is to be expected, but the largest assemblies of particles that would cause noticeable outliers are avoided. The PSD is evaluated on the total recorded number of spots, reported in Table 2.

Figure 11 reports the PSD measured in the 0.8 L/min test and is repeatable across different runs. The experimentally measured values $D_{90}^{exp} = 114$ µm and $D_{10}^{exp} = 49$ µm are very similar to the one expected for the powder *MetcoAdd 316L-D* [18] ($D_{90} = 106$ µm and $D_{10} = 45$ µm). This encouraging result shows that the setup is indeed able to accurately capture the particles. Figure 11 also reports $D_{50}^{exp} = 74$ µm.

The accuracy of this measurement is very dependent on the sharpness of the original images and on the parallax error. The camera setup can be improved by a telecentric lens, and secondarily by a parallel rays light source. Nonetheless, the PSD is essentially spot-on with the values declared by the manufacturer.

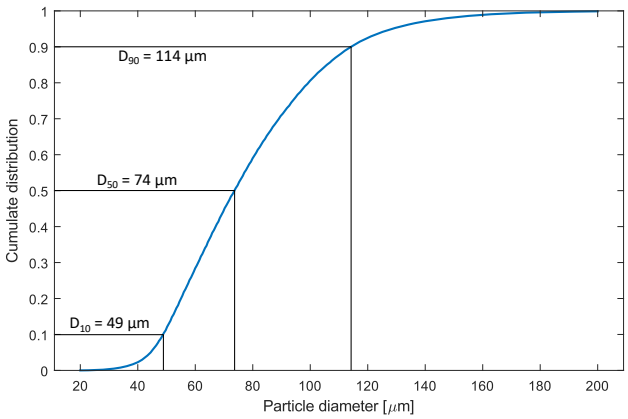

Figure 11. Particle Size Distribution (PSD) measured in the experiments.

4.2. Mass Flow rate Estimation

Figure 12 reports the final results of the particle tracking, calculated using Equation (1). Considering the established flow for $t \geq 0.3$ s, the particles' average velocity remains relatively constant, with a narrow distribution. Indeed, there is a small dependency on the particle loading, as a denser flow determines a slightly lower average velocity, but in this case, the flow rate variation is to be attributed for the most part to the variation in particle concentration.

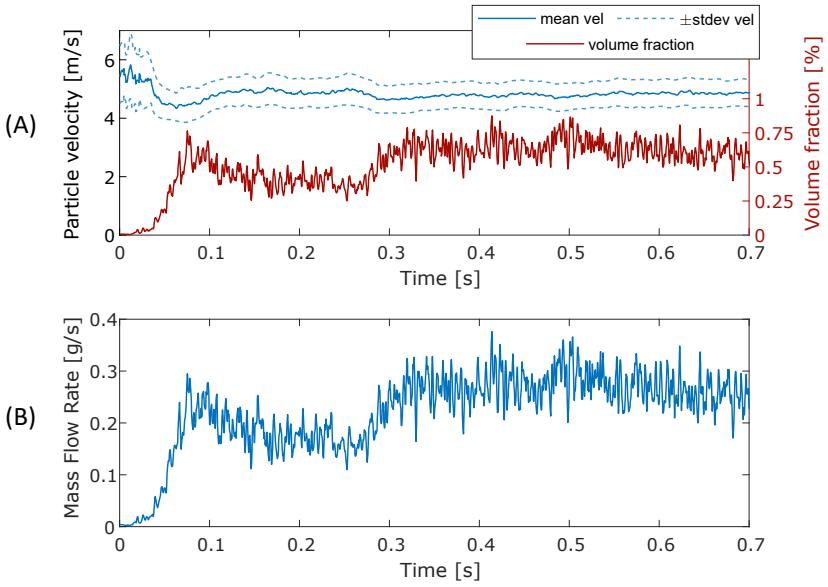

Figure 12. Particle tracking result for a conveying flow of nitrogen of 0.8 L/min, corresponding to an average gas velocity of 12.8 m/s. The diagram reports the particles' velocity distribution and volumetric concentration, averaged over the recorded frame ($L = 3$ mm) and over a moving time window (1 ms) (**A**). These are used to calculate the mass flow rate (**B**).

4.3. Flow Fluctuations

Considering Figure 13, we can evaluate the average of the mass flow rate. The deviation from the average mass flow rate is expressed in terms of the Root Mean Square (RMS), a statistical measure that quantifies the spread or variability of a set of values, or a continuous function, around the average. Assuming a finite number n of virtual measurements, the i-th mass flow rate measurement $\dot{m}_i$ and the average at the outlet $\bar{\dot{m}}_{out}$, the RMS value is defined as

$$\dot{m}_{RMS} = \sqrt{\frac{1}{n}\sum_{i=1}^{n}\left(\dot{m}_i - \bar{\dot{m}}_{out}\right)^2} \tag{3}$$

The results are reported on the same figure and can be compared in Table 3. The intensity of flow irregularities is very close in magnitude to what was determined using CFD-DEM, though with an imperfect match.

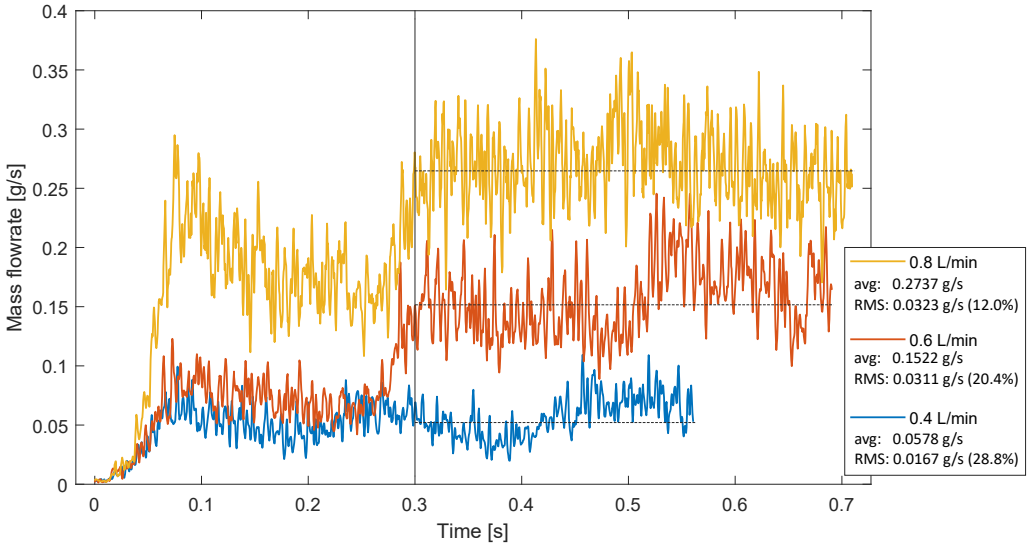

Figure 13. Powder mass flow rate determined using PT for three conditions. The resulting average and RMS values are determined for what are considered as established flow conditions, or $t \geq 0.3$ s.

Table 3. Comparison between experiment and simulation (A, B) [17] of the powder's flow rate (in g/s). The table reports the Reynolds number (see Equation (2)).

Case	CFD-DEM			Experimental			Re
	avg	RMS		avg	RMS		
0.8 L/min – 12.8 m/s				0.2737	0.0323	(12.0%)	971
A : 10 m/s	0.3026	0.0829	(27.4%)				759
0.6 L/min – 9.6 m/s				0.1522	0.0311	(20.4%)	728
0.4 L/min – 6.4 m/s				0.0578	0.0167	(28.8%)	486
B : 5 m/s	0.1541	0.0244	(15.8%)				379

4.4. Photodiode Calibration

The values measured by the photodiode and the differential pressure sensor are reported in Figure 14. The figure shows an evident correlation of all the signals, which suggests the possibility to calibrate inexpensive and small sensors to determine the powder flow rate in positions close to the nozzle.

The signal from the photodiode was directly scaled to the mass flow rate by matching the average values of the two signals between 0.3 s and 0.7 s. This resulted in an extremely good agreement, with the signals almost superimposed, as shown in Figure 15. Evalu-

ating the calibrated flow rate in the stable conditions, or for 0.3 s $\leq t \leq$ 0.7 s, returns RMS $=$ 11.7%, only slightly lower compared to the value determined using PT.

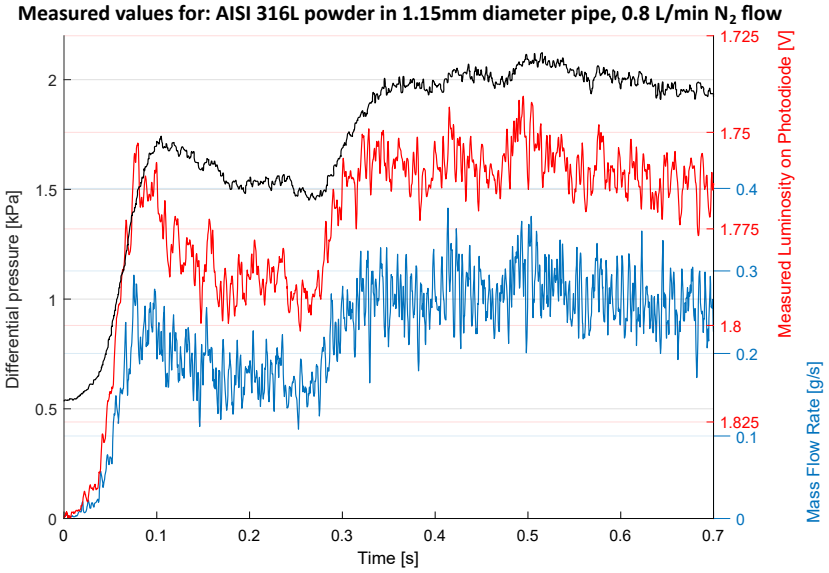

Figure 14. Particles' mass flow rate, for a conveying flow of nitrogen of 0.8 L/min, corresponding to an average gas velocity of 12.8 m/s. The pressure measurement and transmitted luminosity are included, each on the respective axis.

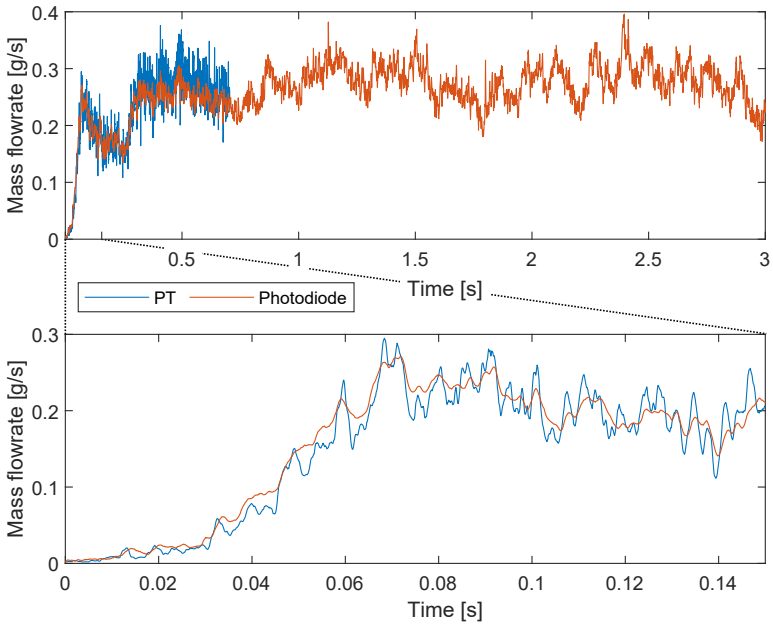

Figure 15. Particles' mass flow rate measured using particle tracking (PT) and the photodiode signal, linearly calibrated, for a conveying flow of 0.8 L/min. The lower panel reports a detail, showing proper signal synchronization.

Even if the acquisition rate was higher, at 50 kHz, the measurement performed via the photodiode shows less steep changes than PT, deriving the physical construction of the device itself. A diode with lower parasitic capacitance, and a better preconditioning circuit, can certainly improve the response time of the sensor, capturing faster varying phenomena. It is unlikely that the photodiode sensing element size, which is 3 $\times$ 3 mm, caused this smoothing; when analyzing the high-speed video, the observed pipe length was a similar value.

4.5. Pressure Measurement

The pressure sensor is an internally compensated and calibrated Integrated Circuit (IC), the values over time are reported in Figure 16. The average values for $t \geq 0.3$ s are calculated, as well as the initial values for the empty pipe.

The experimental values are higher than those obtained by the CFD-DEM simulation [17], reported in Table 4. The simulations are conducted with the hypothesis of laminar flow and Argon gas. Furthermore, the experimental values might be afflicted by localized pressure drops in the proximity of the ports, given the coupler's geometry of Figure 3, which deviates from the ideal.

Table 4. Averaged pressure drop along the conveying pipe for experiment and simulations [17], for both the empty pipe and the established flow conditions. See also Figure 16.

Case	Pressure Drop [Pa/m]				Re
	CFD-DEM		Experimental		
	empty	conveying	empty	conveying	
0.8 L/min - 12.8 m/s			7270	28,350	971
A : 10 m/s	3164	17,584			759
0.6 L/min - 9.6 m/s			5138	14,460	728
0.4 L/min - 6.4 m/s			3300	8937	486
B : 5 m/s	1465	6076			379

The signal is directly affected by the volumetric fraction present in the pipe, but the faster variations are not captured. The differential sensor, connected at the entrance and exit of the pipe, measures the average drop necessary to convey the powder present in the whole pipe. Therefore, even if the sensor declares a response time of 1 ms, the faster variations are averaged over the whole pipe length.

One issue to be aware of when deploying such sensors is that the static port, visible in the coupler of Figure 3, is a few tenths of a mm wide and could become clogged. On the other hand, a visible amount of fine particles were able to pass through the small orifice and make their way through the connecting transparent silicone tube. This could cause issues on the delicate MEMS, which can work in humid conditions but is not qualified in terms of dust protection.

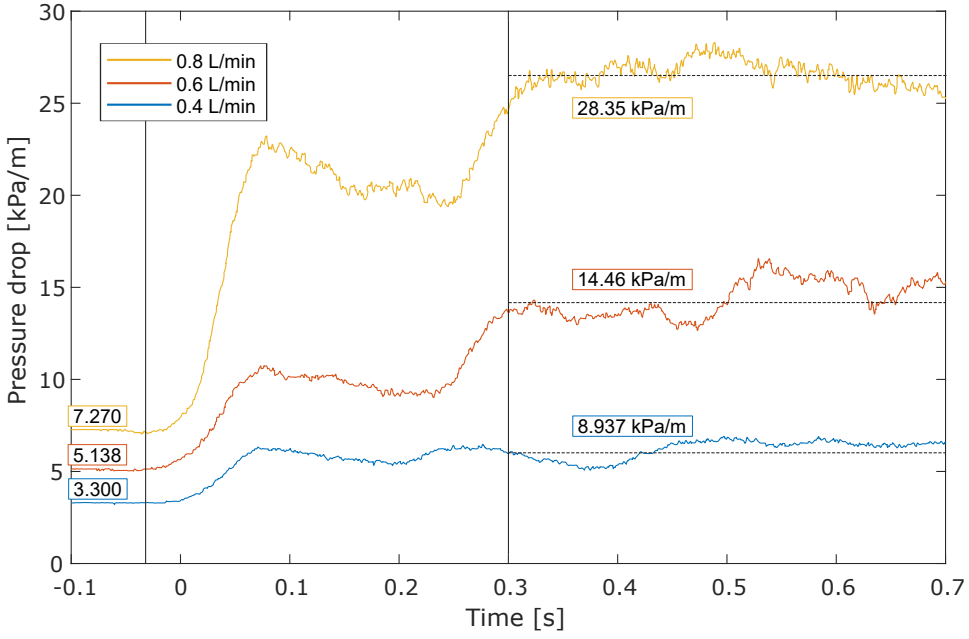

Figure 16. Measured pressure drop along the pipe. The slope is calculated for the nominal pipe length.

5. Discussion

The proposed methodology accurately measures the Particle Size Distribution (PSD), with results consistent with the expected distribution. The accuracy of these measurements is highly dependent on the sharpness of the original images and the parallax error. It is suggested that the camera setup can be improved by using a telecentric lens and a parallel rays light source. Despite these potential improvements, the PSD measurements are repeatable and align closely with the values declared by the manufacturer, validating the image quality of the experimental setup.

Particle velocities are determined experimentally with a high degree of accuracy, using a particle-tracking algorithm. Combined with the measured PSD, the proposed methodology can indirectly measure the powder mass flow rate and volumetric concentration. The measurements have a high temporal resolution, determined by the camera's maximum frame rate at the given resolution, which is 10,000 fps or 10^{-4} s.

The flow rate measurements reveal fluctuations, quantified using the Root Mean Square (RMS) of the deviation from the average in a 2 ms time window, under the conditions identified as established flow. These results are consistent with findings from our previous work on CFD-DEM simulation [17], where similar patterns in mass flow rate and pressure were observed. The values recorded by the experiment and simulations are not an exact match. Nonetheless, the experimental investigation presented in this work provides further information to improve the CFD-DEM simulations.

The photodiode used in the experimental setup shows a high degree of correlation with the measured mass flow rate, and the signal magnitude is linearly proportional to the values measured with the more accurate camera setup. The flow irregularities have lower temporal resolution; therefore, the RMS value reflects this. This reduction in the RMS of flow rate irregularities is especially evident with the pressure measurement, which is nominally acquired every 1 ms and taken over the entire pipe length. This comprehensive measurement effectively averages the observed length, smoothing out the measurement.

6. Conclusions

This study presents a novel methodology for accurately measuring PSD, particle velocities, and flow rate in pneumatic conveying systems, representative of the systems used in DED processes. The results confirm the validity of the proposed approach, with the following key findings:

- The PSD measurements obtained using the high-speed imaging system align closely with the manufacturer's declared values, validating the experimental setup, and while further improvements to the camera setup are suggested, the current methodology is both accurate and repeatable.
- The particle-tracking algorithm successfully measures particle velocities with high temporal resolution (10,000 fps), enabling indirect measurement of powder mass flow rate and volumetric concentration. These measurements provide critical insights into the flow dynamics of the powder.
- Flow rate measurements demonstrate fluctuations, consistent with the trends observed in 2-way coupled CFD-DEM simulations. Although the experimental values and simulation results are not an exact match, the experimental data offer valuable input for refining CFD-DEM models.
- The photodiode measurements show a strong correlation with the more accurate camera-based measurements.
- The proposed method reduces flow irregularities, as indicated by the RMS of flow deviations, particularly in pressure measurements, where averaging over the entire pipe length smooths out the variability.

Overall, this methodology provides a robust framework for improving the consistency of material flow in DED processes. Future work will focus on further refining the

experimental setup and incorporating the insights gained from this study into improved CFD-DEM simulations to enhance the accuracy of flow modeling in industrial applications.

Author Contributions: Conceptualization, L.P.; data curation, L.P.; formal analysis, L.P. and L.F.; funding acquisition, B.A. and A.L. ; investigation, L.P. and L.F.; methodology, L.P.; project administration, L.F., B.A, and A.L.; resources, L.F.; supervision, L.F., B.A. and A.L.; visualization, L.P.; writing—original draft, L. P.; writing—review and editing, L.P., L.F., A.L. and B.A. All authors have read and agreed to the published version of the manuscript.

Funding: This study received financial support from the Basque Government through the Research Group program IT1507-22. This project has received funding from the European Union's Horizon 2020 research and innovation programme under the Marie Skłodowska-Curie grant agreement No. 847624. In addition, a number of institutions back and co-finance this project.

Institutional Review Board Statement: Not applicable.

Informed Consent Statement: Not applicable.

Data Availability Statement: The pre-processed data are available as a Zenodo repository [25]. The Matlab scripts (version 2023a) are available upon request to the corresponding author.

Conflicts of Interest: The authors declare no conflicts of interest.

Abbreviations

The following abbreviations are used in this manuscript:

Nomenclature

DED	Directed Energy Deposition
LMD	Laser Metal Deposition.
CFD-DEM	Computational Fluid Dynamics - Discrete Element Modeling.
PSD	Particle Size Distribution.
DEM	Discrete Element Modeling.
MP-PIC	Multi-Phase Particle In Cell.
DPMs	Discrete Particle Models.
PT	Particle Tracking.
RMS	Root Mean Square.
Re	Reynolds Number.
MEMS	Micro Electro-Mechanical System.
OFJ	OpenFOAM Journal.
SSC	Honeywell SSCDRRN100MDAA5 Pressure Sensor.

Mathematical Symbols

ρ_g	Gas Density.
$\overline{u}$	Average Gas Velocity.
d	Pipe Diameter.
μ	Dynamic Viscosity.
D_{10}	10th percentile of the PSD.
D_{50}	50th percentile of the PSD.
D_{90}	90th percentile of the PSD.
$\dot{m}$	Mass Flow Rate.
ϕ	Volumetric Concentration.
V_{tot}	Total Observed Volume.
$\hat{v_Z}$	Average Velocity Along Pipe.

Appendix A. Kalman Tracking Initialization

In the Jaquaman linking step of the tracker, the software needs to look for possible *targets* for each *origin* spots in order to initiate a track. The search radius, by default, is centered on the origin spot and must be relatively large to account for the movement. After

the track is initiated, the next search circles can be much smaller thanks to the predictive step of the Kalman filter.

In the fast flows, initiating a track is not optimal, as the spots might move a lot in a preferential direction, leading to an impractically large search radius. Most of the initiated tracks ended up being incorrect and terminated only after one or two steps. The presence of these artifact tracks also impedes the initiation of the true tracks, and therefore some visually very clear cases are ignored. In the end, only few tracks per frame were visible, and most particles were unable to be traced.

To solve this issue, the TrackMate plugin [21] was modified in order to include a manual first guess. In this strategy, the Jaquaman linking step of the tracker sees the unmodified target spot, but the origin spot is translated by a displacement vector, specified as manual input. Moving the origin spots closer to the expected position of the target spots allows for a much smaller initial search radius, increasing the efficacy of the Jaquaman linking step. After determining the relation between an origin and a target spot, the tracking can then proceed using the unmodified Kalman filter. The modification has been submitted to the public repository of the plugin at https://github.com/trackmate-sc/TrackMate/pull/296 (accessed on 20 July 2024).

The improvement in tracking the particles in this situation is evident and reported in the table of Figure A1, without which the particle tracking was rather inefficient. The difference in the number of total recognized spots is negligible, and only due to the fact that the filtering on the particle size is performed through sliders instead of text input. The greatest difference is in the number of edges and tracks, which means that there is more information on the movement. However, more importantly, before the improvement, there were several tracks moving in unpredictable directions, as seen in the image, which is incorrect. In the new implementation, the tracks are, on average, much longer, and span the whole length of the window, denoting a correct tracking.

	Before	After
ine Spots	259364	247619
Edges	63346	129730
Tracks	9867	17678

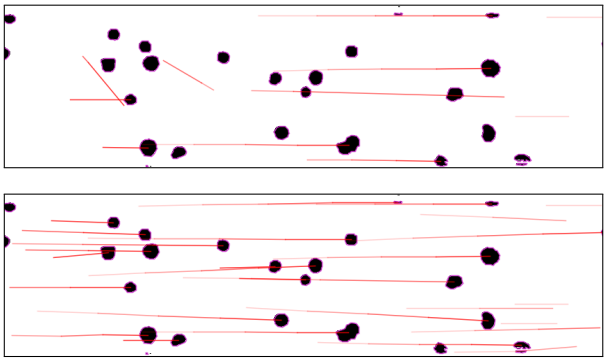

Figure A1. Enhancement in particle-tracking capabilities in the same test recording.

Appendix B. Particle Volume Estimation

The computational model assumes spherical particles, which, when projected onto a plane, create circular shadows that may overlap. As observed in Figure 8, some overlapping particles are not involved in the tracking but need to be considered to evaluate the volume accurately. The following method reduces the error using a simple algebraic model, which could be further improved with additional data, potentially using an artificial neural network (ANN) or more rigorous mathematical definitions. However, the current method already provides satisfactory results under the presented conditions.

The equations describing relationships for the perimeter, area, and volume for a system composed of multiple circular objects (in 2D) or spherical objects (in 3D), each with radius R_i are

$$\begin{cases} P = 2\pi \sum R_i = 2\pi n R_{\text{eq}} \\ A = \pi \sum R_i^2 = \pi n R_{\text{eq}}^2 \\ V = \dfrac{4}{3}\pi \sum R_i^3 = \dfrac{4}{3}\pi n R_{\text{eq}}^3 \end{cases} \tag{A1}$$

They express the idea that the total perimeter, area, and volume can be represented by equivalent sums of the contributions of individual objects with a mean or effective radius R_{eq} and a total number of objects n. The objective is to attempt to estimate V from the first two, P and A, deriving R_{eq} and n.

From the perimeter and area, we derive R_{eq} as

$$\begin{cases} R_{\text{eq}} = \dfrac{P}{2\pi n} \\ R_{\text{eq}}^2 = \dfrac{A}{\pi n} \\ R_{\text{eq}} = \sqrt{\dfrac{A}{\pi n}} \end{cases} \tag{A2}$$

Equating the expressions for R_{eq}

$$\begin{cases} \dfrac{P}{2\pi n} = \sqrt{\dfrac{A}{\pi n}} \\ n = \dfrac{P^2}{4\pi A} \end{cases} \tag{A3}$$

Divide area and perimeter to find R_{eq}

$$\begin{cases} \dfrac{A}{P} = \dfrac{\pi n R_{\text{eq}}^2}{2\pi n R_{\text{eq}}} \\ R_{\text{eq}} = \dfrac{2A}{P} \end{cases} \tag{A4}$$

At this point, n and R_{eq} can be used to find the volume

$$\begin{cases} V = \dfrac{4}{3}\pi n R_{\text{eq}}^3 \\ \quad = \dfrac{4}{3}\pi \left(\dfrac{P^2}{4\pi A} \right) \left(\dfrac{2A}{P} \right)^3 \\ \quad = \dfrac{8}{3}\pi \dfrac{A^2}{P} \end{cases} \tag{A5}$$

This method has an error proportional to the overlap. Considering only two particles: from no overlap, where the error is theoretically zero, the real area and volume are underestimated by half when both particles are exactly the same size and completely overlapped. If the particles are different sizes, the error is less than that. This is verified using the script `circleOverlapSimulation.m`, resulting in Figure A2. The error at distance greater than 1 disappears for more dissimilar sizes, and the global error reduces for more dissimilar sizes. The worst case scenario is for an equal radius, where both estimated values are half of the real area and volume when both particles are totally overlapped. If only one circle is evaluated (or $R_2 \to 0$), the formula is exact. This discrepancy is to be expected and a correction would need to be applied; it was decided to avoid applying further hypotheses for a marginal improvement that anyway would not account for slightly oval, elongated, or joined particles.

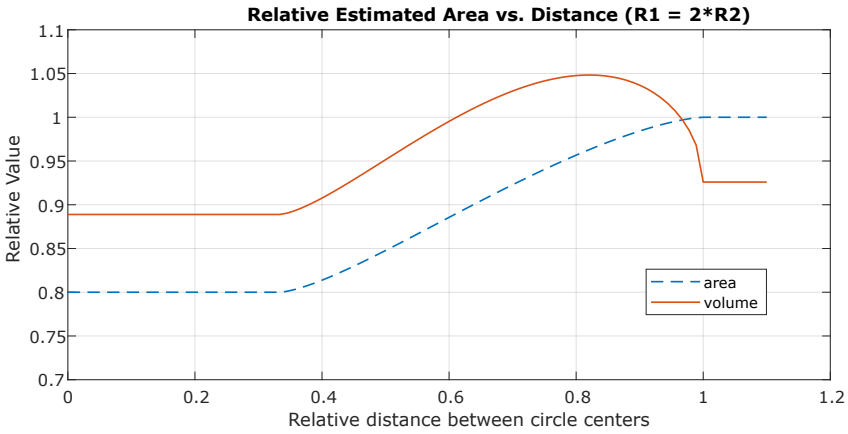

Figure A2. Relative values of volume and area estimated using the measured apparent area and perimeter of overlapping disks.

References

1. Singh, A.; Kapil, S.; Das, M. A comprehensive review of the methods and mechanisms for powder feedstock handling in directed energy deposition. *Addit. Manuf.* **2020**, *35*, 101388. [CrossRef]
2. Dadbakhsh, S.; Hao, L.; Kong, C. Surface finish improvement of LMD samples using laser polishing. *Virtual Phys. Prototyp.* **2010**, *5*, 215–221. [CrossRef]
3. Murer, M.; Furlan, V.; Formica, G.; Morganti, S.; Previtali, B.; Auricchio, F. Numerical simulation of particles flow in Laser Metal Deposition technology comparing Eulerian–Eulerian and Lagrangian–Eulerian approaches. *J. Manuf. Process.* **2021**, *68*, 186–197. [CrossRef]
4. Zekovic, S.; Dwivedi, R.; Kovacevic, R. Numerical simulation and experimental investigation of gas–powder flow from radially symmetrical nozzles in laser-based direct metal deposition. *Int. J. Mach. Tools Manuf.* **2007**, *47*, 112–123. [CrossRef]
5. Mezhericher, M.; Brosh, T.; Levy, A. Modeling of Particle Pneumatic Conveying Using DEM and DPM Methods. *Part. Sci. Technol.* **2011**, *29*, 197–208. [CrossRef]
6. Baraldo, S.; Roncoroni, A.; Palo, F.; Valente, A. Multi-physics based methodology for evaluating powder feeding quality for Laser Metal Deposition. *Procedia CIRP* **2022**, *107*, 623–628. [CrossRef]
7. Higashitani, K.; Makino, H.; Matsusaka, S. *Powder Technology Handbook*; CRC Press, Taylor & Francis Group: Boca Raton, FL, USA , 2020.
8. Levy, A. *Handbook of Conveying and Handling of Particulate Solids*; Elsevier: Amsterdam, The Netherlands; New York, NY, USA, 2001; pp. 403–409. [CrossRef]
9. Thornton, C. *Granular Dynamics, Contact Mechanics and Particle System Simulations: A DEM Study*; Springer-Verlag GmbH: Berlin/Heidelberg, Germany, 2015; p. 195.
10. Klinzing, G.E.; Rizk, F.; Marcus, R.; Leung, L.S. *Pneumatic Conveying of Solids: A Theoretical and Practical Approach*, 3rd ed.; Springer Nature: Dordrecht, The Netherlands, 2010.
11. Mills, D. *Handbook of Pneumatic Conveying Engineering*; Marcel Dekker: New York, NY, USA, 2004.
12. Zhou, F.; Hu, S.; Liu, Y.; Liu, C.; Xia, T. CFD—DEM simulation of the pneumatic conveying of fine particles through a horizontal slit. *Particuology* **2014**, *16*, 196–205. [CrossRef]
13. Zhao, H.; Zhao, Y. CFD—DEM simulation of pneumatic conveying in a horizontal channel. *Int. J. Multiph. Flow* **2019**, *118*, 64–74. [CrossRef]
14. Li, L.; Huang, Y.; Zou, C.; Tao, W. Numerical Study on Powder Stream Characteristics of Coaxial Laser Metal Deposition Nozzle. *Crystals* **2021**, *11*, 282. [CrossRef]
15. Sommerfeld, M. Analysis of collision effects for turbulent gas-particle flow in a horizontal channel: Part I. Particle transport. *Int. J. Multiph. Flow* **2003**, *29*, 675–699. [CrossRef]
16. Song, Z.; Li, Q.; Li, F.; Chen, Y.; Ullah, A.; Chen, S.; Wang, W. MP-PIC simulation of dilute-phase pneumatic conveying in a horizontal pipe. *Powder Technol.* **2022**, *410*, 117894. [CrossRef]
17. Pedrolli, L.; Achiaga Menor, B.; Martinez de Arenaza, I.; López, A. Comparison of CFD-DEM and MP-PIC in the Simulation of Metal Powder Conveying for Laser Metal Deposition. *OpenFOAM® J.* **2024**, *4*, 26–40. [CrossRef]
18. Oerlikon. *Datasheet of Gas-Atomized Powder MetcoAdd 316L-D*; Oerlikon: Pfäffikon, Switzerland. Available online: https://mymetco.oerlikon.com/en-us/product/metcoadd316ld (accessed on 20 July 2024). .
19. Honeywell International Inc. *Honeywell TruStability™SSC Pressure Sensors;* Honeywell International Inc.: Charlotte, NC, USA.
20. Schindelin, J.; Arganda-Carreras, I.; Frise, E.; Kaynig, V.; Longair, M.; Pietzsch, T.; Preibisch, S.; Rueden, C.; Saalfeld, S.; Schmid, B.; et al. Fiji: An open-source platform for biological-image analysis. *Nat. Methods* **2012**, *9*, 676–682. [CrossRef] [PubMed]
21. Tinevez, J.Y.; Perry, N.; Schindelin, J.; Hoopes, G.M.; Reynolds, G.D.; Laplantine, E.; Bednarek, S.Y.; Shorte, S.L.; Eliceiri, K.W. TrackMate: An open and extensible platform for single-particle tracking. *Methods* **2017**, *115*, 80–90. [CrossRef] [PubMed]

22. Jaqaman, K.; Loerke, D.; Mettlen, M.; Kuwata, H.; Grinstein, S.; Schmid, S.L.; Danuser, G. Robust single-particle tracking in live-cell time-lapse sequences. *Nat. Methods* **2008**, *5*, 695–702. [CrossRef] [PubMed]
23. Spinewine, B.; Capart, H.; Larcher, M.; Zech, Y. Three-dimensional Voronoï imaging methods for the measurement of near-wall particulate flows. *Exp. Fluids* **2003**, *34*, 227–241. [CrossRef]
24. Ayachit, U. *The ParaView Guide*; Full Color Version ed.; Kitware Inc.: Clifton Park, NY, USA, 2015.
25. Pedrolli, L. Optical Particle Tracking in the Pneumatic Conveying of Metal Powders through a Thin Capillary Pipe. *Preprints* **2024**, 2024080385. [CrossRef]